Resistive switching in an organic supramolecular semiconducting ferroelectric

Nicolas M. Casellas, Indre Urbanaviciute, Tim Cornelissen, Jose Augusto Berrocal, Tomas Torres, Martijn Kemerink and Miguel Garcia-Iglesias

Journal Name

COMMUNICATION

Resistive switching in an organic supramolecular semiconducting ferroelectric

Received 00th January 20xx,
Accepted 00th January 20xx

DOI: 10.1039/x0xx00000x

www.rsc.org/

Nicolás M. Casellas,[a, b] Indre Urbanaviciute,[d] Tim Cornelissen,[d] José Augusto Berrocal,[e] Tomás Torres,*[a, b, c] Martijn Kemerink,*[d] Miguel García-Iglesias*[a, b]

The combination of switchable dipolar side groups and the semiconducting core of the newly synthetized C_3-symmetric benzotrithiophene molecule (BTTTA) leads to an ordered columnar material showing continuous tunability from injection- to bulk-limited conductivity modulation.

Organic non-volatile memory devices based on ferroelectricity represent a promising approach towards the development of a low-cost, efficient and mechanically robust bendable memory technology.[1] However, an important drawback of these materials is the insulating nature of most ferroelectrics, necessitating a destructive information read-out.[2] The combination of ferroelectric and semiconducting properties in one functional material emerges as a valuable solution to this problem, where the bistable ferroelectric polarization serves as an on-off switch, while the semiconducting functionality allows for the given logical state to be probed as a high or low conductivity. This bifunctionality was first achieved by blending distinct semiconducting and ferroelectric molecules.[3] Nevertheless, the possibility to prepare such materials out of a single molecular component is highly desirable since the interplay between the ferroelectric and the semiconducting properties would take place at the molecular level, diminishing phase segregation between different molecules.[4]

Supramolecular chemistry arises as a highly effective tool to construct highly ordered self-assembled functional materials combining both properties. To the date, either semiconducting[5] or ferroelectric self-assembled columnar organic materials have been described. In this context, among amide-based ferroelectric materials,[6] C_3-symmetrical benzene-1,3,5-tricarboxamides (BTAs) present excellent properties due to their clear Curie-Weiss behavior,[7] saturating polarization with excellent retention,[8] low electrical fatigue and a broad operational temperature range.[8,9] One of the main advantages of this type of materials is their excellent tunability via molecular structure modification,[8,9] opening the possibility to use π-conjugated central cores to access new organic semiconducting-ferroelectrics.[10,11] Hence, the applied molecular designs consist of π-conjugated central aromatic cores, functionalized with amide moieties for self-assembly and aliphatic tails to favour solubility and liquid-crystalline behaviour. Applying this molecular design, some of us reported two examples of amide-based ferroelectrics with different semiconducting conjugated cores, exhibiting unprecedented 'ferro-conductive' functionality due to coexisting and interacting ferroelectricity and semiconductivity. The materials reported showed resistive switching based on different mechanisms, including either charge injection barrier modulation (IBM)[10] or, a previously unobserved, bulk conductivity switching (BCS).[11]

Herein we demonstrate the feasibility of this approach with a C_3-symmetric benzotrithiophene tricarboxamide (**BTTTA**) molecule which self-assembles via threefold H-bonding into columnar liquid crystalline mesophases (Fig. 1). The proximity of the amide dipoles to the semiconducting core[12] of a highly ordered homeotropically aligned material boosts the hybridization of ferroelectric and semiconducting properties. This unique interplay makes our BTT-cored trisamide the first single material to show both injection- and bulk-limited conductivity modulation while simultaneously demonstrating superior ferroelectric properties.

The newly synthesized **BTTTA** (Fig. 1) was prepared in high yield in multigram scale (see ESI for synthetic characterization).

The self-assembly of **BTTTA** molecule in the solid state was characterized by different techniques. The presence of

[a] Department of Organic Chemistry, Universidad Autónoma de Madrid (UAM), Calle Francisco Tomás y Valiente, 7, 28049 Madrid, ES. E-mail: tomas.torres@uam.es, miguel.iglesias@uam.es.
[b] IMDEA Nanociencia, c/ Faraday 9, Cantoblanco, 28049, ES.
[c] Institute for Advanced Research in Chemical Sciences (IAdChem), UAM, 28049 Madrid, ES.
[d] Complex Materials and Devices, Department of Physics, Chemistry and Biology (IFM), Linköping University, 58183 Linköping, Sweden. E-mail: martijn.kemerink@liu.se
[e] Institute for Complex Molecular Systems, Eindhoven University of Technology, P. O. Box 513, 5600 MB Eindhoven, The Netherlands.
Electronic Supplementary Information (ESI) available: [details of any supplementary information available should be included here]. See DOI: 10.1039/x0xx00000x

hydrogen-bonding interactions was confirmed by infrared spectroscopy (IR). **BTTTA** presents N-H vibrations around 3244 cm^{-1} and amide vibrations at 1626 and 1554 cm^{-1} in the solid state, confirming the formation of three-fold hydrogen bonded aggregates (Fig. S1).[12]

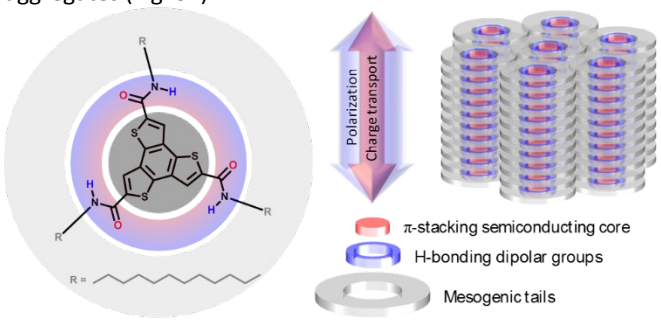

Fig. 1. (a) **BTTTA** molecule and schematic representation of its self-assembly into columnar aggregates. Semiconducting BTT cores provide a channel for efficient charge transport, while surrounding switchable dipolar amide moieties induce polarization-coupled modulation. Mesogenic sidechains supply required molecular mobility and solubility.

Moreover, UV-VIS spectra in chloroform and in spin-coated films present a BTT core absorption band less intense and blue-shifted with respect to the absorption maximum of the molecularly dissolved state observed in THF solutions, pointing to the monomer stacking in form of H-aggregates[13] (see Fig. S2). The thermal properties and the liquid crystalline (LC) behavior of **BTTTA** were assessed by Differential Scanning Calorimetry (DSC), Temperature Dependent Wide Angle X-Ray Scattering (TD-WAXS), Temperature Dependent Infrared spectroscopy (TD-IR) and Polarized Optical Microscopy (POM).

Table 1. Phase behavior of **BTTTA**.

		T °C (ΔH kJ/mol) [a]					
heating	Cr	52 (19.1)	Col_{sq}	160 (11.2)	Col_{hd}	266 (62.2)	I
cooling	Cr	17 (31.3)	Col_{sq}	173 (12.8)	Col_{hd}	267 (70.1)	I

[a] Onset temperatures and transition enthalpies are reported based on the first cooling and second heating run in DSC (10 °C/min). The observed phases are: Cr = crystalline, Col_{sq} = disordered square cubic LC, Col_{hd} = disordered hexagonal columnar LC, I = isotropic liquid.

Three phase transitions are visible in the DSC traces of **BTTTA** (Table 1 and Fig. S3). **BTTTA** undergoes a first intense transition from isotropic to the LC mesophase, at approximately the same temperature upon heating or cooling (267°C). This transition is associated with a high enthalpy 79 kJ mol^{-1}, which represents an additional evidence of the H-bonding formation, being comparable with structurally similar derivatives reported.[12] Interestingly, **BTTTA** exhibits a second weak transition around 165°C. This transition was assigned by WAXS measurements to a liquid crystalline phase change from columnar hexagonal to square cubic mesophase showing reflections with a relative reciprocal spacing of 1:√3:2:√7 and 1:√2:2:√6, respectively (Fig. S4 and Table S1). Finally, a clearly detectable supercooling effect of ~35°C was observed during crystallization in the cooling-heating DSC experiments.

Further insights into the bulk morphology of **BTTTA** were obtained by TD-WAXS measurements observing a clear increase of interdisc distances (3.5 Å to 4.1 Å) with increasing temperature (Fig. S4 and Table S1). This common phenomenon in columnar discotic mesophases was ascribed by TD-IR to the weakening of the hydrogen-bonds between discs upon increasing temperature by following the progressive broadening and shift to higher wavenumbers of the N-H stretching and the evolution of the amide I vibration from 1621 cm^{-1} to 1629 cm^{-1}(Fig. S5).[12] Examination of the phase by POM confirmed the findings from DSC and XRD. The aliphatic **BTTTA** is solid below 15°C, and up to 260°C it is liquid crystalline where pseudo-focal conic patterns of columnar mesophases were observed (see Fig. S6).

Thin-film spin-coated devices with non-injecting electrodes were prepared to examine the ferroelectric properties of the material. (see SI, section II and Fig. S7 for further details). The measured ferroelectric hysteresis loops were of a close-to-ideal shape over a broad temperature range, see Fig. 2a, and full polarization saturation with increasing field was observed, see Fig. S8a. Thus, any secondary non-ferroelectric inputs can be ruled out.[14] Negligible injection current was observed in these Al/BTTTA/Al devices. The remnant polarization was found to be around 25 mC m^{-2}, which matches the geometrically expected value for an ideal square cubic lattice with a constant dipole moment per molecule of 3×4 D,[15] which corroborates its ferroelectric origin. In addition, **BTTTA** demonstrates the typical butterfly-shaped small-signal capacitance-voltage characteristics (Fig. S8b, see also SI, Section V). The remnant polarization is virtually temperature-independent in the range 25–130°C; in contrast, and as expected,[8] the coercive field increases roughly linearly with cooling, see Fig. S8c. Comparing this coercive field trend to previously published results of the analogous BTA-C12 molecule having a smaller benzene core,[9] it is evident that the dependence is steeper, and the coercive field value is higher for the **BTTTA** at the same conditions. On basis of kinetic Monte Carlo simulations we attribute this to subtle differences in molecular packing in combination with improved self-assembly in **BTTTA** (Fig. S9, SI Section VII).

Turning to the kinetic polarization switching properties of **BTTTA**, we find that the coercive field dependence on the field sweeping frequency and the polarization switching time versus the applied field can be rationalized in terms of thermally-activated nucleation-limited switching (TA-NLS, see Fig. S11b and d) .[16] The lognormal switching current transients (Fig. S11c) suggest a nucleation-limited polarization switching mechanism, also characteristic to BTAs.[7,17] This proves that the material behaves as a regular ferroelectric showing a polarization switching time is in the sub-millisecond range at elevated temperatures.

The depolarization kinetics are, however, significantly slower than any of the previously tested amide-based molecular ferroelectrics, which results in strongly improved polarization retention, see Fig. 2b. The depolarization kinetics of **BTTTA** fit well to a stretched exponential function $\propto \exp[-(t/\tau)^{\beta}]$ with a stretching exponent $\beta \approx 0.05$–0.1; similar low values were observed in a strongly branched (1-hexylheptyl tail) BTA-C6/7[18]

and, interestingly, in quasi-atomistic kinetic Monte Carlo simulations.[8] At 120°C the polarization retention of **BTTTA** is ~7 orders of magnitude longer than the best reported BTAs,[8] and around 13 orders of magnitude longer than P(VDF:TrFE), see Fig. S8d. If compared to its neat analogue dodecyl-tailed BTA-C12, the improvement becomes 8–10 orders of magnitude, see Fig. 2b. Note that at room temperature no depolarization could be observed.

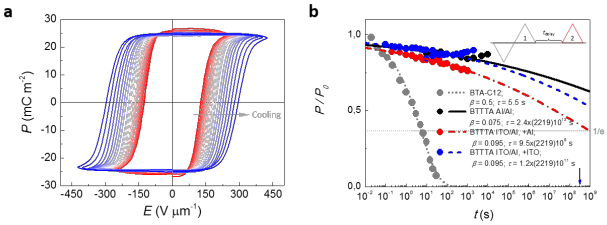

Fig. 2. (a) Temperature dependence of the polarization hysteresis loops. Data obtained at an applied field frequency of 25 Hz upon cooling from 130°C (red) to room temperature (blue) on a device with blocking Al electrodes. (b) Polarization retention of Al/Al (solid black line), of ITO/Al with biased Al (red dash-dotted line) and of ITO/Al with biased ITO (blue dashed line) capacitor devices of BTTTA. Data of benzene-cored analogue BTA-C12 at 120°C is given as a grey dotted line for comparison. Depolarization kinetics fit well to a stretched exponential function (stretching exponent β and time constant values τ). The blue arrow indicates 10 years. The measurement scheme is given in the inset, where '1' is the full-poling preparation step and '2' is the lost polarization probing step.

The reason for the record polarization stability of **BTTTA** likely lies in the high-level structural ordering, as also seen in the WAXS measurements. As discussed above, due to the large conjugated cores, large molecular self-assemblies are formed in the **BTTTA** material layers (see Fig. S11), which leads to a reduced number of nucleation centres for polarization switching (=defects). As polarization switching in this material is driven and limited by nucleation, having fewer defects reduces the possibility for polarization reversal resulting in higher coercive fields and suppressed depolarization. The much stronger improvement in polarization retention (over 9 orders of magnitude) compared to the increase in the coercive field in **BTTTA** devices can be explained by the different sensitivity of these processes to the decreased disorder. Cornelissen *et al.* have demonstrated by 3D kinetic Monte-Carlo simulations that nucleation of the field-driven polarization switching is localized at the electrode interfaces, whereas depolarization is governed by bulk defects.[19] Therefore, high structural order allows for significant improvement in polarization retention with only a slight concomitant increase in the coercive field, which is highly appealing from the application perspective.

To summarize the results so far, **BTTTA** is a textbook-like ferroelectric with remnant polarization corresponding to the permanent dipole density. Moreover, **BTTTA** shows the best polarization retention among the amide-based molecular ferroelectrics reported to date, which exceeds the commercial requirement of 10 years already at high temperatures.

Taking into account the experimental energy orbitals of BTTTA obtained by cyclic voltammetry (CV) using ferrocene as internal standard (see Fig. S10), we take $E_{HOMO} \approx -5.5$ eV and $E_{LUMO} \approx -2.1$ eV during the resistive switching experiments (Fig. S7).[12] The dark *J-V* curves for a symmetric Au/Au device in Fig. 4a are an excellent example of bulk conductivity switching as sketched in Fig. 3a (see discussion in SI, Section VIII), with both the 'on' and 'off' states operating in the space-charge-limited current (SCLC) regime (Fig. S12a). The extracted hole transport mobilities 10^{-9}–10^{-8} cm^2 V^{-1} s^{-1} for these out-of-plane devices are in the same range as for similar materials,[10,11] yet can be strongly improved to reach ~10^{-4} cm^2 V^{-1} s^{-1} in in-plane interdigitated electrode devices, see Fig. S13 and SI, Section IX; the latter values are likely still limited by structural imperfections. The probing frequency dependence (~0.0015–0.015 Hz from red to blue in Fig. 4a) reveals a clear shift of the on-to-off turning point towards higher fields, which corresponds to the coercive field versus frequency trend of the ferroelectric, see Fig. S11b. This switching point is less sharp than in the idealized case (Fig. 3a) due to the inherent (Preisach) distribution in coercive fields typical to real ferroelectrics.[17] The noticeably lower coercive field value compared to that obtained from the pure ferroelectric characterization can be explained by the low field sweeping rates, see Fig. S11b.

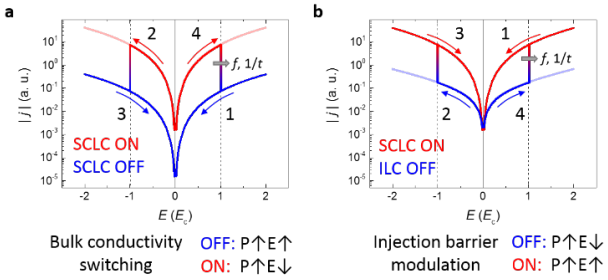

Fig. 3. Schematics of *j-E* characteristics typical for different resistive switching mechanisms. (a) Bulk conductivity switching (BCS) with space-charge limited current (SCLC) both at the 'on' and 'off' states. (b) Injection barrier modulation (IBM) with SCLC at the 'on' state and injection-limited current at the 'off' state. In both cases, the on/off switching event occurs at the coercive field E_c of the ferroelectric, which increases with the applied field frequency.

When an energy barrier for charge injection is introduced, the bulk-limited conductivity switching is conquered by injection barrier modulation (IBM) and an 'off' to 'on' state transition is observed at the coercive field, *cf.* Fig. 3b and Fig. 4c. The data resembles those reported before for α-CBT.[10]

In principle, due to the opposite conditions for the 'on' and 'off' states, IBM and BCS are competing mechanisms. In Fig. 4b we show that, at favourable circumstances, they can both be observed in a similar Al/Au device. At increasing positive bias, the IBM 'on' current is subsequently reduced by the competing BCS. This intermediate, double-switching regime can be seen even clearer when moving beyond the quasi-static regime (Fig. S14, Section X). In both Fig. 4b and Fig. S14a charge injection is negligible whilst the polarization direction opposes the (forward) field, that is, when the injection barrier is present. Once the coercive field is approaching and the polarization begins to switch, charge injection is enabled. This results in a rapid growth of the current density, which at higher biases is turned off due to the BCS regime becoming dominant. The average transported charge, measured in quasi-static mode (Fig. S14b), grows quadratically with the applied forward field, as expected for SCLC. This behaviour is maintained throughout a temperature range of 125°–25°C, see Fig. S14c.

The possibility to observe these two effects in a single *J-V* measurement stems from their different field dependencies. At low fields, IBM is expected to be dominant because partial polarization reversal that typically nucleates at the electrodes may be sufficient to overcome the injection barrier and the device can immediately jump to the 'on' state.

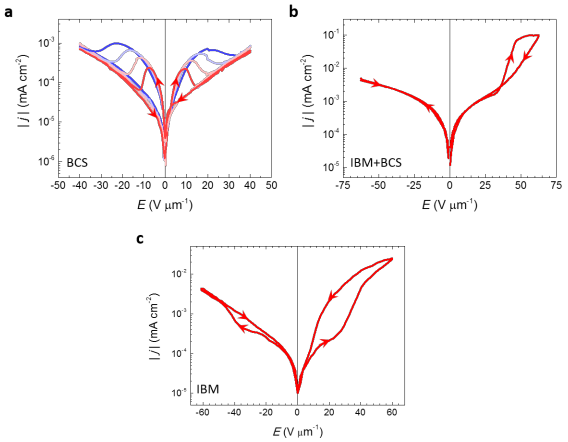

Fig. 4. Quasi-static j-E characteristics measured on BTTTA. Depending on the injection barrier governed by the electrode material, BTTTA may demonstrate (a) bulk conductivity switching if no injection barrier is present, (c) injection barrier modulation if the barrier height is optimized to be overcome with ferroelectric polarization. (b) Manifestation of both (a) and (c) mechanisms is possible, depending on the injection barrier and the position of the coercive field. A current offset due to displacement has been subtracted.

The BCS regime on the other hand requires an almost completed polarization switching to fully reach the off-state due to percolation effects steering currents around low-conductivity regions.

As ferroelectric polarization and depolarization might be affected by the injected charges and the contact potential difference, we also checked the polarization retention in these asymmetric electrode devices. However, as before both forward (blue) and reverse (red) bias show depolarization time constants exceeding the 10-year limit.

We have demonstrated a new material, **BTTTA**, with a unique combination of semiconducting and ferroic properties. These include an unprecedented interplay between bulk- and injection-limited conductivity switching due to the coupling of the ferroelectric dipoles to both the bulk and interfacial charge transport. The dominant mechanism depends on the relation between the height of the electrode-determined injection barrier (if any) and the coercive voltage of the ferroelectric. The characteristic SCLC charge transport mobilities reach ~10^{-4} cm^2 V^{-1} s^{-1}. Moreover, **BTTTA** shows an extreme polarization stability even at 120°C, being superior to the commercially available material P(VDF:TrFE), which is notoriously sensitive to elevated temperatures. These characteristics are an outcome of optimization by rational design of the molecular structure, where solubility and molecular mobility are kept in good balance with semiconducting and ferroelectric properties.

Financial support from MINECO, Spain (CTQ2017-85393-P) (T.T.) is acknowledged. I.U. acknowledges funding by Vetenskapsrådet. T. D. C. acknowledges financial support from the Swedish Government Strategic Research Area in Materials Science on Functional Materials at Linköping University (Faculty Grant SFO Mat LiU No. 2009 00971).

Conflicts of interest

There are no conflicts to declare.

Notes and references

1 P. Heremans, G. H. Gelinck, R. Müller, K.-J. Baeg, D.-Y. Kim and Y.-Y. Noh, *Chem. Mater.*, 2011, **23**, 341.
2 J. C. Scott and L. D. Bozano, *Adv. Mater.*, 2007, **19**, 1452.
3 K. Asadi, D. M. de Leeuw, B. de Boer and P. W. M. Blom, *Nat. Mater.*, 2008, **7**, 547.
4 K. Asadi, M. Li, P. W. M. Blom, M. Kemerink and D. M. de Leeuw, *Mater. Today*, 2011, **14**, 592.
5 T. Wöhrle, I. Wurzbach, J. Kirres, A. Kostidou, N. Kapernaum, J. Litterscheidt, J. C. Haenle, P. Staffeld, A. Baro, F. Giesselmann and S. Laschat, *Chem. Rev.*, 2016, **116**, 1139.
6 a) K. K. Bejagam, C. Kulkarni, S. J. George and S. Balasubramanian, *Chem. Commun.*, 2015, **51**, 16049. b) A. L. Goodwin, N. P. Funnell, K. P. van der Zwan, C. S. Zehe, H.-W. Schmidt, K. Kreger and J. A. Hill, J. Senker, *Angew. Chemie Int. Ed.*, 2017, **56**, 4432.
7 A. V. Gorbunov, T. Putzeys, I. Urbanavičiūtė, R. A. J. Janssen M. Wübbenhorst, , R. P. Sijbesma, M. Kemerink, *Phys. Chem. Chem. Phys.*, 2016, **18**, 23663.
8 I. Urbanavičiūtė, S. Bhattacharjee, M. Biler, J. A. M. Lugger, T. D. Cornelissen, P. Norman, M. Linares, R. P. Sijbesma, Martijn Kemerink, *Phys. Chem. Chem. Phys.*, 2019, **21**, 2069.
9 a) I. Urbanavičiūtė, X. Meng, M, T. D. Cornelissen, A. V. Gorbunov, S. Bhattacharjee, R. P. Sijbesma, M. Kemerink, *Adv. Electron. Mater.*, 2017, **3**, 1600530.
10 A. V Gorbunov, A. T. Haedler, T. Putzeys, R. H. Zha, H.-W. Schmidt, M. Kivala, I. Urbanavičiūtė, M. Wübbenhorst, E. W. Meijer, M. Kemerink, *ACS Appl. Mater. Interfaces*, 2016, **8**, 15535.
11 A. V Gorbunov, M. García-Iglesias, J. Guilleme, T. D. Cornelissen, W. S. C. Roelofs, T. Torres, D. González-Rodríguez, E. W. Meijer, M. Kemerink, *Sci. Adv.*, 2017, **3**, e1701017.
12 A. Demenev, S. H. Eichhorn, T. Taerum, D. F. Perepichka, S. Patwardhan, F. C. Grozema, L. D. A. Siebbeles and R. Klenkler, *Chem. Mater.*, 2010, **22**, 1420.
13 N. M. Casellas, S. Pujals, D. Bochicchio, G. M. Pavan, T. Torres, L. Albertazzi, M. García-Iglesias, *Chem. Commun.*, 2018, **54**, 4112.
14 X. Meng, A. V. Gorbunov, W. S. Christian Roelofs, S. C. J. Meskers, R. A. J. Janssen, M. Kemerink and R. P. Sijbesma, *J. Polym. Sci. Part B Polym. Phys.*, 2017, **55**, 673.
15 C. Kulkarni, S. K. Reddy, S. J. George and S. Balasubramanian, *Chem. Phys. Lett.*, 2011, **515**, 226.
16 M. Vopsaroiu, J. Blackburn, M. G. Cain and P. M. Weaver, *Phys. Rev. B*, 2010, **82**, 24109.
17 I. Urbanavičiūtė, T. D. Cornelissen, X. Meng, R. P. Sijbesma and M. Kemerink, *Nat. Commun.*, 2018, **9**, 4409.
18 A. V Gorbunov, X. Meng, I. Urbanaviciute, T. Putzeys, M. Wübbenhorst, R. P. Sijbesma and M. Kemerink, *Phys. Chem. Chem. Phys.*, 2017, **19**, 3192.
19 T. D. Cornelissen, M. Biler, I. Urbanavičiūtė, P. Norman, M. Linares and M. Kemerink, *Phys. Chem. Chem. Phys.*, 2019, **21**, 1375.